A&A 541, A19 (2012)
DOI: 10.1051/0004-6361/201118537

Astronomy & Astrophysics

Evolution of dust in the Orion Bar with *Herschel*[⋆]

I. Radiative transfer modelling

H. Arab[1], A. Abergel[1], E. Habart[1], J. Bernard-Salas[1], H. Ayasso[1], K. Dassas[1], P. G. Martin[2], and G. J. White[3,4]

[1] Institut d'Astrophysique Spatiale (IAS), UMR8617, CNRS/Universite Paris-Sud, 91405 Orsay, France
e-mail: `heddy.arab@ias.u-psud.fr`
[2] Canadian Institute for Theoretical Astrophysics, Toronto, Ontario, M5S 3H8, Canada
[3] The Rutherford Appleton Laboratory, Chilton, Didcot OX11 0QX, UK
[4] Department of Physics & Astronomy, The Open University, Milton Keynes MK7 6 AA, UK

Received 28 November 2011 / Accepted 7 February 2012

ABSTRACT

Context. Interstellar dust is a key element in our understanding of the interstellar medium and star formation. The manner in which dust populations evolve with the excitation and the physical conditions is a first step in comprehending the evolution of interstellar dust.
Aims. Within the framework of the Evolution of interstellar dust *Herschel* key programme, we have acquired PACS and SPIRE spectrophotometric observations of various photodissociation regions, to characterise this evolution. The aim of this paper is to trace the evolution of dust grains in the Orion Bar photodissociation region.
Methods. We used *Herschel*/PACS (70 and 160 μm) and SPIRE (250, 350 and 500 μm) together with *Spitzer*/IRAC observations to map the spatial distribution of the dust populations across the Bar. Brightness profiles were modelled using the DustEM model coupled with a radiative transfer code.
Results. Thanks to *Herschel*, we are able to probe in great detail the dust emission of the densest parts of the Orion Bar with a resolution from 5.6″ to 35.1″. These new observations allow us to infer the temperature of the biggest grains at different positions in the Bar, which reveals a gradient from ~70 K to 35 K coupled with an increase of the spectral emissivity index from the ionization front to the densest regions.
Combining *Spitzer*/IRAC observations, which are sensitive to the dust emission from the surface, with *Herschel* maps, we were able to measure the Orion Bar emission from 3.6 to 500 μm. We find a stratification in the different dust components that can be quantitatively reproduced by a simple radiative transfer model without dust evolution (diffuse interstellar medium abundances and optical properties).
However, including dust evolution is needed to explain the brightness in each band. Polycyclic aromatic hydrocarbon (PAH) abundance variations, or a combination of PAH abundance variations with an enhancement of the biggest grain emissivity caused by coagulation give good results. Another hypothesis is to consider a length of the Bar along the line of sight different at the ionization front than in the densest parts.

Key words. infrared: ISM – dust, extinction – photon-dominated region (PDR) – ISM: individual objects: Orion Bar – radiative transfer

1. Introduction

Interstellar grains constantly interact with their surrounding gaseous environment. They also strongly interact with radiation, absorbing the UV/visible photons from stars and re-emitting the energy in the infrared range. Their emission wavelength range depends on both the grain size and composition. To study the dust properties and their evolution, many models have been developed in the last two decades to reproduce the dust emission spectrum and the extinction curve (e.g., Desert et al. 1990; Zubko et al. 2004; Draine & Li 2007; Compiègne et al. 2011). Most of these use three dust components to reproduce the observational constraints: polycyclic aromatic hydrocarbons (PAHs), "very small grains" (VSGs), and big grains (BGs). The two first are made of carbonaceous particles. Owing to their sizes (~[0.4−10] nm), they are stochastically heated and emit most of their energy below 60 μm. The BGs (up to ~200 nm) are in thermal equilibrium with the radiation field and contain most of the dust mass. During their life, dust grains undergo modification of their size, structure and chemical composition. To understand this evolution, we need to trace the characteristics of grains in relation to changes of the physical and dynamical properties.

Photo-dissociation regions (PDRs) are the surface layers where the radiation field is able to dissociate H_2 molecules but cannot ionize hydrogen atoms. Consequently, they are found at the interface of HII regions and molecular clouds. In these zones, the radiation field coming from nearby OB stars regulates the physical and chemical evolution of the gas. That is why PDRs are the favourite laboratories to study evolution of the dust and gas constituents with the local excitation and the physical conditions.

The Orion Bar has been extensively observed, leading to a large dataset in different tracers of the gas component (e.g., White & Sandell 1995; van der Werf et al. 1996; Walmsley et al. 2000; Goicoechea et al. 2011). Located between the Trapezium cluster and the Orion Molecular Cloud, the Bar is part of the Orion nebula and lies at 414 ± 7 pc away from

---

[⋆] *Herschel* is an ESA space observatory with science instruments provided by European-led Principal Investigator consortia and with important participation from NASA.

the Earth (Menten et al. 2007). The incident radiation field is dominated by the O6 star θ^1 Ori C and has been estimated to $G = [1{-}4] \times 10^4\ G_0$ at the ionization front (Marconi et al. 1998; Tielens & Hollenbach 1985) where G_0 is the integrated intensity of the standard interstellar radiation field (ISRF) given by Habing (1968).

Observational studies of the bright Bar have been accompanied by several modelling studies to determine its physical structure, excitation, and gas emission. Previous studies revealed different layers within the PDR, with a stratified structure typical of an edge-on geometry (e.g., Tielens et al. 1993; Tauber et al. 1994; Lis & Schilke 2003). HCO^+ and HCN $J = 1{-}0$ emission line maps from Young Owl et al. (2000) showed the presence of dense clumps ($n_H = 3 \times 10^6$ cm^{-3}) embedded in an interclump medium with a density $n_H \approx 5 \times 10^4$ cm^{-3}, which emits most of the intensity.

Within the framework of the "Evolution of interstellar dust" *Herschel* key programme (Abergel et al. 2010), the Orion Bar has been observed by the ESA *Herschel* Space Observatory (Pilbratt et al. 2010). Its unprecedented spatial resolution together with its spectral coverage at the far-infrared wavelengths allow us to probe the dust evolution within PDRs. The broad sensitivity range and the spectrophotometric capabilities of PACS (Poglitsch et al. 2010) and SPIRE (Griffin et al. 2010) detectors give a unique view of the Orion Bar at the far-infrared wavelengths. Several papers by our group deal with *Herschel* observations of the Orion Bar. Bernard-Salas et al. (2012) focused on PACS spectroscopic data whereas Habart et al. (in prep.) explore SPIRE/FTS observations. In this paper, we present the photometric maps from PACS and SPIRE to study the emission of dust at thermal equilibrium with the radiation. We seek to address the following questions: what are the processes involved in the dust evolution in the Orion Bar? Are there abundance variations from the diffuse ISM? And are there any differences in the optical properties of the grains in the Bar compared to grains in the diffuse ISM?

Section 2 describes the photometric data from SPIRE and PACS, explaining how they were reduced. In Sect. 3, the morphology of the Orion Bar in the *Spitzer* and *Herschel* bands is presented. These new observations allow us to study the evolution of the BG spectral energy distribution across the Orion Bar (Sect. 4), but also to probe dust emission by mapping its spatial distribution (Sect. 5). In Sect. 6, we model the dust emission in the Orion Bar using the DustEM model (Compiègne et al. 2011) coupled with a radiative transfer code, which is compared to our data. The results are discussed in Sect. 7.

2. Observations and data processing

The Orion Bar was mapped during the *Herschel* Science Demonstration Phase (SDP) on February 23, and March 11, 2010 using the PACS (70 and 160 μm) and SPIRE photometers (250, 350 and 500 μm). For PACS, two concatenated and perpendicular $12' \times 12'$ scan maps (corresponding to two obsIds) were observed using the medium scan speed ($20''$/s), a scan length of $12'$, a cross-scan step of $50''$, and a 15 scan legs (total observing time 1726 s). For SPIRE, a single map was taken without a repetition (total observing time of 193 s).

2.1. Data processing

The SPIRE maps reported in this paper are the Level 2 naive maps delivered by the *Herschel* Space Center (HIPE version 7.0.1991), with standard corrections for instrumental effects and glitches. Striping induced by offsets in the flux calibration from one detector to another was removed using the Scan Map Destriper module included in the HIPE environment. The overall absolute flux accuracy is dominated by the calibration uncertainty and is conservatively estimated to be ±7%[1].

The PACS data were processed with HIPE (version 6.0.1196) with special care for deglitching and the removal of the $1/f$ noise component. For each filter, processing from Level 0 to Level 1 is performed on each obsId and yielded one Level 1 frame by obsId. A second-level glitch mask was computed from preliminary maps built from the frames after high-pass median filtering. Object masks were also attached to the Level 1 frames. These were computed from the preliminary maps (using the second-level glitch mask) to flag the brightest parts of the sky on the high-pass filtering step performed from Level 1 to Level 2 (see below).

The processing from Level 1 to Level 2 combines the two Level 1 frames to obtain one final map for each filter. The $1/f$ noise component was removed with high-pass median filtering, using the glitch mask and the object mask. To avoid any filtering of extended emission, we have taken a relatively broad window size, corresponding to five times the scan length. Finally, we performed a simple coaddition of the data. The overall absolute flux accuracy is estimated to be ±20% (Ali 2011) for both the blue and red bands, corresponding to the conservative value for extended sources.

The maps from our *Herschel* programme are shown in Fig. 1 with the 3.6 μm IRAC observation (from the *Spitzer* Data Archive). The zero point of *Herschel* maps is unknown, therefore, a background emission centred around the position α_{J2000} = 5h35min26.7s and $\delta_{J2000} = -5°26'4.7''$ and corresponding to emission unrelated to the Bar was subtracted from the data. This point is not critical for our analysis given the high brightness of the Orion Bar compared to the background emission. The five processed maps are publicly available (`http://idoc-herschel.ias.u-psud.fr/sitools/client-user/`).

2.2. Beam effects

To make a coherent spatial study and extract spectral energy distributions (SEDs), all maps need to be brought in the same beam, in our case the 500 μm beam. The simplest way to do that is to assume that *Herschel* beams are Gaussian. Therefore each map is usually convolved by a Gaussian whose full width at half maximum (FWHM) is given by

$$\mathrm{FWHM} = \sqrt{\mathrm{FWHM}_2^2 - \mathrm{FWHM}_1^2}, \tag{1}$$

where FWHM_1 is the FWHM of the considered beam and FWHM_2 is the FWHM of the larger beam of the dataset. Nevertheless, simulations and measurements of *Herschel* point spread functions (PSFs) show that the real beams are significantly different from Gaussian since they present asymmetries and secondary lobes (Sibthorpe et al. 2011). This point is particularly critical since ignoring secondary lobes misestimates the fluxes at the edges of bright structures, as illustrated in Fig. 2. Therefore, it is necessary to take into account the real shape of the beam in our study, and we used the theoretical PSFs delivered by the *Herschel* Science Centre. The transition functions needed

---

[1] From the SPIRE observers' manual, available on the webpage: `http://Herschel.esac.esa.int/`

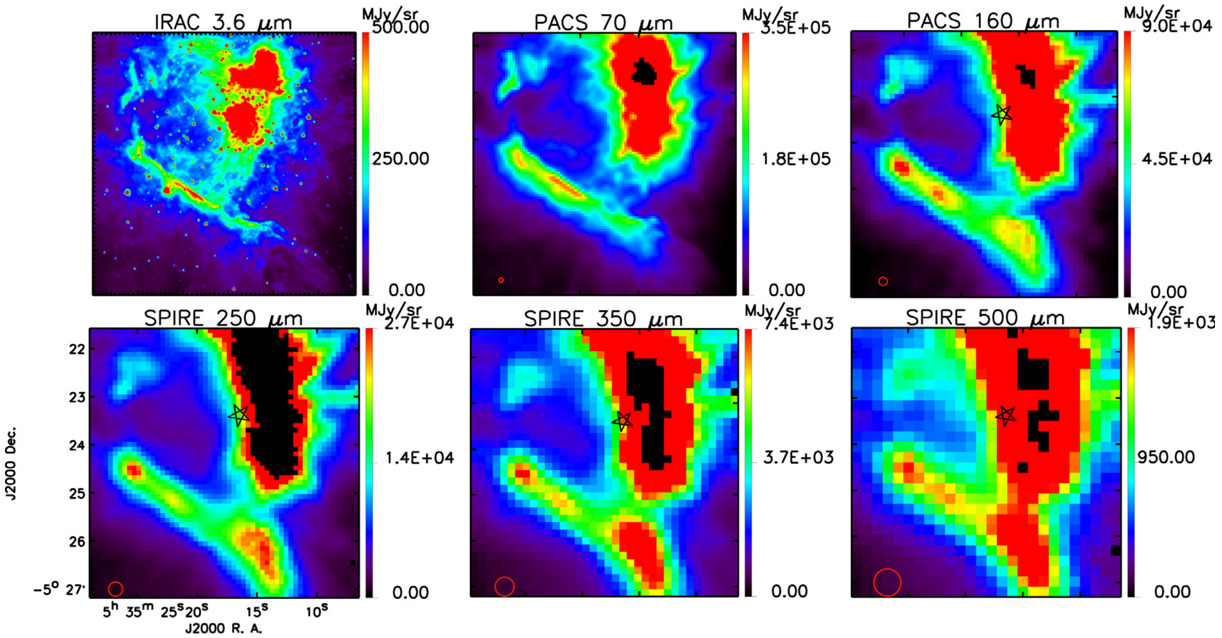

Fig. 1. Orion Bar maps observed by the IRAC, PACS and SPIRE instruments. The red circle in the left corner stands for the FWHM for each channel, and the black star shows the location of the illuminating source. The saturated pixels are indicated in black.

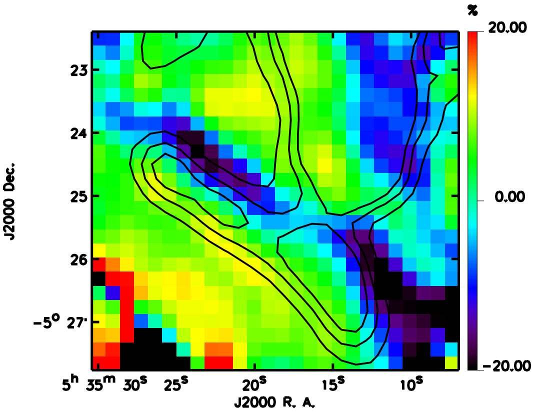

Fig. 2. $(I_{250\,\mu\mathrm{m}} * h(x, FWHM) - I_{250\,\mu\mathrm{m}} * \hat{k}_{250->500}) / (I_{250\,\mu\mathrm{m}} * \hat{k}_{250->500})$: relative differences between the 250 μm observation brought to the 500 μm resolution using a 30.4″ FWHM Gaussian and the transition PSF obtained with our method; black contours show the 250 μm emission (levels: 10 500, 14 000, 17 500 MJy sr^{-1}).

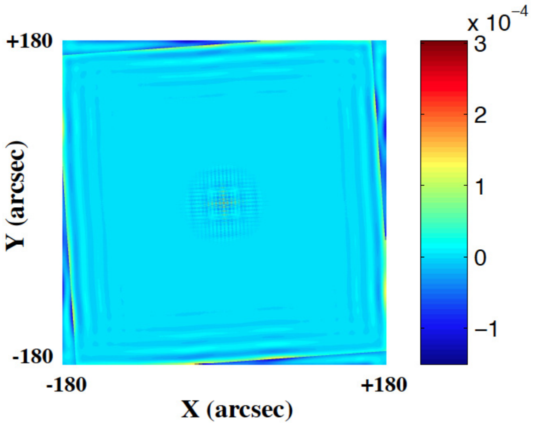

Fig. 3. Relative error in the reconstruction of the SPIRE 500 μm from the 250 μm one using our inversion method: $(\mathrm{PSF}_{500} - \mathrm{PSF}_{250} * \hat{k}_{250->500})/\max(\mathrm{PSF}_{500})$.

to convolve the maps to a common beam size do not have an analytical form, and must be numerically calculated.

Computing a transition function k between two PSFs, $\mathrm{PSF}_2 = \mathrm{PSF}_1 * k$, is a deconvolution problem (Gonzalez & Woods 1992). We chose a regularised least-squares method (Tikhonov 1963) to compute a transition PSF k from a given channel of PSF$_1$ to PSF$_2$:

$$\hat{k} = \arg\min J(k) = \|\mathrm{PSF}_2 - \mathrm{PSF}_1 * k\|_2^2 + \mu\,\|\Omega(k)\|_2^2\,, \qquad (2)$$

where Ω is a smoothness function taken as a derivative in our case, and μ is the regularisation parameter, which can be fixed according to the noise level present in both PSFs. A transition PSF corresponds to a couple of channels for a given observation because the orientation angles of the instruments are required in the computation. Recently, Aniano et al. (2011) have proposed common-resolution convolution kernels based on another method. In their approach, the low-pass filtering, needed to avoid problems in the high-frequency component, is made by a filter whose shape is fixed whatever the considered beams. In our method the filtering is optimised by adapting the filter according to the shape of the considered PSFs, thus the transition function computed is optimal in the least-squares sense. Thanks to regularisation process, this method is able to give a very good reconstruction of k, respecting the balance between spectral information available in the PSFs and the noise levels (Fig. 3). We present the *Herschel* observations convolved to the 500 μm resolution and gridding in Fig. 4.

3. Morphology of the Orion Bar with *Herschel*

We have mapped the emission of the BGs, which trace the matter up to the densest regions of the Orion Bar. Indeed, with *Spitzer*/IRAC, we only detected the emission of the smallest dust particles, which is strongly dependent on the radiation field since they are stochastically heated. Therefore, we observed the emission coming from the surface of dense regions. This is illustrated

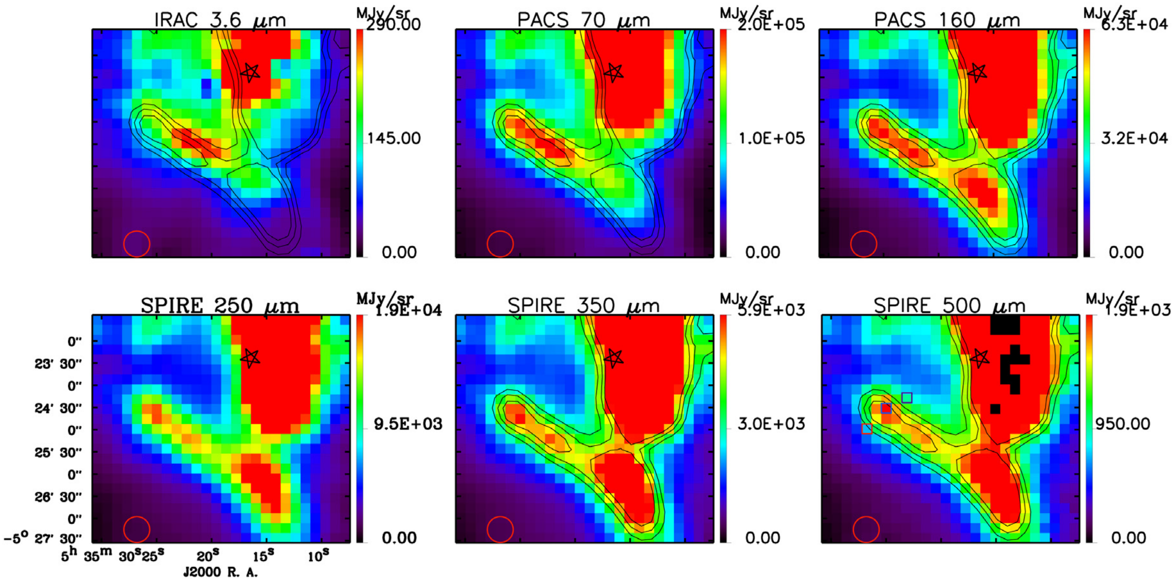

Fig. 4. Observed maps convolved to the 500 μm beam (red circle; *FWHM* = 35.1″) using the inversion method described Sect. 2.2. The three-colour squares on the 500 μm observation stand for the positions of the three SEDs shown Fig. 5. Black contours show the 250 μm emission convolved to the 500 μm beam (red circle) with levels at 10 000, 12 500 and 15 000 MJy sr^{-1}.

Table 1. Contribution of VSGs to the overall intensity (in %) according to the DustEM model[a] in the five *Herschel* bands for the spectra shown in Fig. 5.

Offset from the 500 μm peak position (5h35min16s;−5°23′23″)	70 μm	160 μm	250 μm	350 μm	500 μm
(+28″, −14″) (top panel of Fig. 5)	4.1	3.5	3.6	4.0	5.4
(0″, 0″) (middle panel of Fig. 5)	4.0	2.4	2.3	2.6	2.7
(−28″, +28″) (low panel of Fig. 5)	4.2	2.0	1.9	2.1	2.2

Notes. (a) We use the same dust populations as in Compiègne et al. (2011) and an excitation corresponding to θ^1 Ori C.

by the first panel of Fig. 1. The 3.6 μm map from *Spitzer*/IRAC exhibits numerous narrow bright filaments caused by the illuminated edge of the Bar. These bright filaments contain small-scale structures, revealing the complexity of the edge of the Bar.

In *Herschel* bands, it is striking to note that the general structure of the Bar appears the same (Fig. 1), especially if we look at the maps brought to the same resolution (Fig. 4). Even if the ridge appears broader because of resolution effects, the shape is the same and we recognize the sub-structure along the Bar seen with IRAC. However, because we are sensitive to BGs and denser matter, we see several differences in the sub-structure. For example, the south-west part of the Bar ends with a bright cloud that is invisible at shorter wavelengths, indicating the presence of cold material. Besides, the sub-structures detected along the Bar have not the same relative brightness at different wavelengths. The brightest one at 70 μm is the faintest at 250 μm, revealing a strong difference of temperature. Finally, we observed with *Herschel* an increase of the distance between the observed Bar and the illuminating star with increasing wavelength.

With these new *Herschel* observations, combined with *Spitzer*/IRAC data, we are able to study the spectrum of the BG emission and to make a coherent spatial study of the different dust populations in the Orion Bar.

4. BG spectrum

The PACS and SPIRE data allow us to derive the BG component spectrum at each position on the Bar. After convolving all maps to the 500 μm beam, we fitted a modified blackbody to the extracted spectra according to

$$I_\nu = \tau_{\nu_0} \left(\frac{\nu}{\nu_0}\right)^\beta B_\nu(T), \tag{3}$$

where I_ν is the specific intensity, τ_{ν_0} is the dust optical depth at frequency ν_0, β is the spectral emissivity index, B_ν is Planck's function, and T is the dust temperature. The fits were performed using the *MPFIT* IDL function (Markwardt 2009), which relies on the Levenberg-Marquardt algorithm. The free parameters τ_{ν_0}, β and T were computed for each pixel of the maps. The five bands were included in the fits because BGs dominate in all bands. This has been verified with the DustEM model, which is able to quantify the contribution of non-equilibrium emission at a given wavelength (Table 1).

Errors entered in the fits are conservative and correspond to the calibration uncertainties (20% for PACS and 7% for SPIRE) because the statistical noise is negligible compared to calibration errors. The fitted spectra were integrated over the instrument filters to take the colour correction into account. We can then study the behaviour of the BG spectrum at different positions in the cloud. Figure 5 shows the evolution of the BG spectrum while crossing the PDR. The exact positions are shown by the coloured squares in Fig. 4. In front of the Bar (top panel of Fig. 5), the fitted temperature is 71 ± 10 K, whereas as we enter into the bright ridge, it decreases sharply to 49 ± 4 K (middle panel of Fig. 5). Behind the Bar (low panel of Fig. 5), BGs cool down to 37 ± 2 K. The β spectral emissivity index follows an inverse behaviour, increasing from 1.2 to 2.2. This trend is real but might be amplified by the mixture of grains of different temperature along the line of sight. Indeed, mixing can significantly broaden and flatten the modified blackbody shape. This effect is more pronounced in front of the Bar, where the geometry is not edge-on (purple spectrum). Thanks to the high resolution of *Herschel* observations, we are able to probe T and β variations on small spatial scales ($\sim$35″), in a single and transition object for the first time. A full study of T and β in the Orion Bar region will be presented in detail and compared to previous results in a second paper (Arab et al., in prep.).

5. Brightness profiles

Using the *Herschel* data coupled with *Spitzer*/IRAC observations, we have been able to study the spatial variations of the different dust populations. The BG emission was probed by *Herschel* bands, whereas the 3.6 μm emission from IRAC was used as a proxy of the PAHs. The 8 μm channel, usually taken as a tracer of aromatic emission, is affected by saturation. Besides, *Herschel* resolution offers the opportunity to resolve the BG emission within the Orion Bar.

We extracted brightness profiles obtained along a cut going from the exciting star through the PDR, whose position is visible in Fig. 7. The Orion Bar appears as a prominent peak in these cross-cuts, lying at $\sim$2′ from θ^1 Ori C (Fig. 6). Sub-structure in this profiles appears at 3.6 and 70 μm, showing that the Bar is more complicated than a simple ridge. A shift between the peak positions is also clearly visible. This shift is real, as can be seen on the comparison of the 250 μm map superimposed with contours of the 3.6 μm map after convolution and reprojection, as described above (Fig. 7). The 250 μm emission clearly rises further from the exciting star than the 3.6 μm one. This can be generalised: the shorter the wavelength, the closer to the exciting source is the emission. Since we probed bigger grains at longer wavelengths, we saw that the BG emission is located farther away from the ionization front than the emission from the smaller grains. Moreover, in Fig. 7 we show the C^{18}O emission observed by the SPIRE-FTS (Habart et al., in prep.), which traces the dense matter, and a good correlation is observed with the 250 μm broadband emission, confirming that the FIR dust emission is a tracer of the densest part of the PDR (see also Buckle et al. 2012).

The ionization front is located at 111″ from θ^1 Ori C (Pellegrini et al. (2009) from [SII] intensity profile; Bernard-Salas et al. (2012) from [NII] PACS observations). Adopting the same cut as Bernard-Salas et al. (2012), we find from the 3.6 μm emission that PAHs peak at 116 ± 2″ from the star, just behind the ionization front. We lack good VSG tracers since 24 μm *Spitzer*/MIPS data of this region are unusable because of saturation and the 70 μm PACS emission is dominated by BGs. The peak of the BG emission is around 150″ away from the exciting star. The fact that the emission of different species rises successively when we enter the PDR is a result of the nearly edge-on orientation of the Orion Bar (see also Dicker et al. 2009).

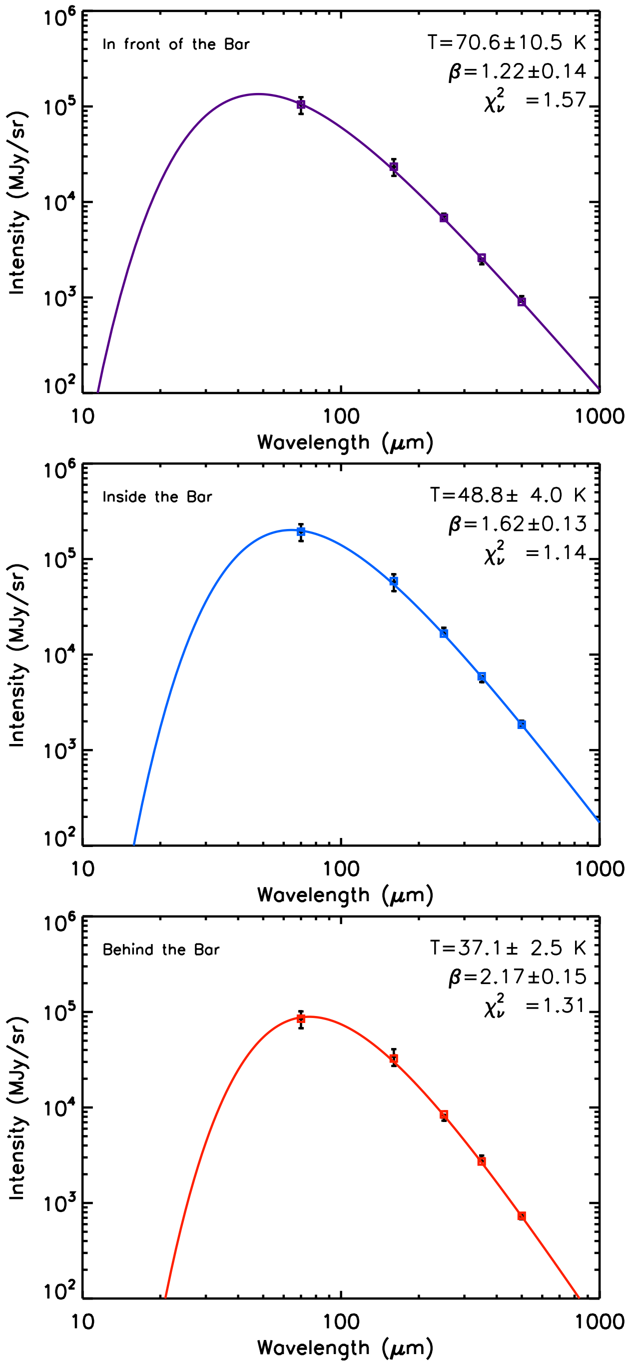

Fig. 5. Modified blackbody fits at different positions across the Bar. Reduced χ^2 is indicated on each fit. The position of each SED is indicated in the 500 μm panel of Fig. 4.

6. Modelling

The Orion Bar is a very dense PDR that is illuminated by a strong radiation field, therefore the dust size distribution and optical properties should show some differences to those seen towards diffuse regions. Our goal is to extract evidence of this evolution, and to characterise and quantify it. However, radiative transfer effects have a crucial influence on the dust emission, which is why modelling is needed to recover the properties of grains in the Orion Bar.

6.1. Model description

We modelled the brightness profiles using the DustEM code for the dust emission coupled with a plane-parallel radiative transfer code.

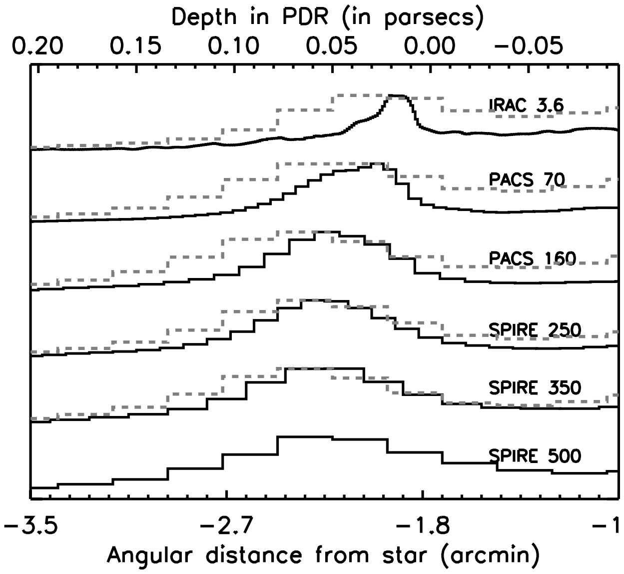

Fig. 6. Normalised brightness profiles across the Orion Bar at native resolution (black solid lines) and convolved to the 500 μm (grey dashed lines). The resolution of the solid line profiles corresponds to the nominal resolution of each instrument: 1.88″ for IRAC, 5.6″ for PACS 70 μm, 11.3″ for PACS 160 μm, 17.6″ for SPIRE 250 μm, 23.9″ for SPIRE 350 μm, 35.1″ for SPIRE 500 μm.

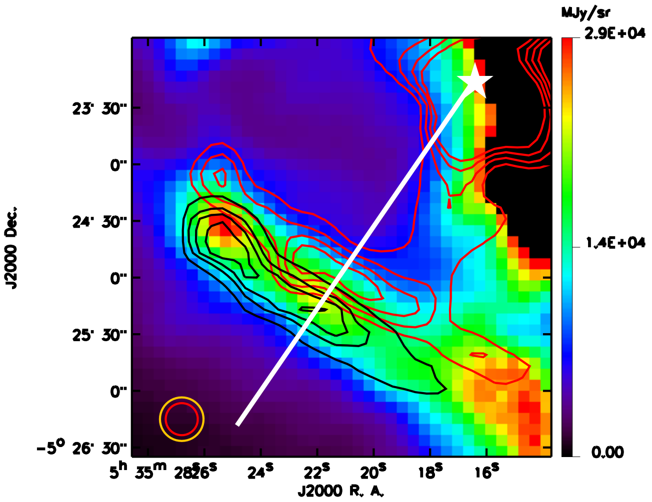

Fig. 7. *Herschel* 250 μm observation (colour image) and IRAC 3.6 μm map (red contours) in the SPIRE 250 μm beam (red circle; *FWHM* = 17.6″). Black contours show the distribution of $C^{18}O$ (8−7) observed with the SPIRE-FTS (yellow circle; *FWHM* = 23.9″) from Habart et al. (in prep.). The white star illustrates the position of θ^1 Ori C and the white line is the cut of Fig. 6.

DustEM (Compiègne et al. 2011) is a numerical tool that calculates the emission of an ensemble of dust populations of various properties under the effect of a given radiation field. The dust model we used includes four different populations: PAHs, small amorphous carbons (SamC), large amorphous carbons (LamC), and astronomical silicates (aSil). The dust abundances and emissivities used in the model are indicated in Table 2. The reader is referred to Fig. 1 of Compiègne et al. (2011) for a detailed description of the size distribution and to Figs. 4 and 5 in the same paper to examine the computed extinction curve. In PDRs, the evolution of the physical conditions is dominated by the changes in the radiation field. Therefore the radiative transfer effects are critical for our study and need to be properly quantified. We used the model described in Compiègne et al. (2008) to take them into account. In this model, the PDR is represented by a semi-infinite plane-parallel slab whose density is defined by the user. The cloud is illuminated by the Mathis ISRF (Mathis et al. 1983), plus a blackbody-radiation field derived from stellar parameters of θ^1 Ori C (radius and distance to the PDR). Then the code computes the flux $F(z, \lambda)$:

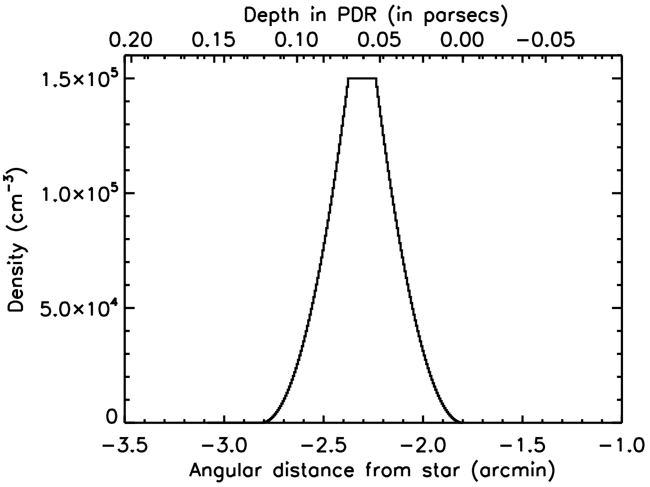

Fig. 8. Density profile with a power-law rise and a symmetric fall-off. The maximum density is 1.5×10^5 cm^{-3} and is reached at 5.25×10^{-2} pc far from the PDR edge.

$$F(z, \lambda) = F_t(z, \lambda) + F_b(z, \lambda) + F_{IR}(z, \lambda), \tag{4}$$

where z is the depth in the PDR, λ is the wavelength, $F_t(z, \lambda)$ is the transmitted flux, $F_b(z, \lambda)$ is the backscattered one, and $F_{IR}(z, \lambda)$ denotes the emission coming from low-depth dust, which absorbs, re-emits and thus heats the grains located deeper in the PDR. The calculation was performed assuming an asymmetry parameter for the scattering phase function g of 0.6, which corresponds to the commonly employed value for the diffuse ISM (Witt et al. 1997). Moreover, the model only considers a single backscattering, in other words, when a photon is backscattered, it cannot return to the densest part of the PDR. This approximation is justified because the g value indicates a strong forward scattering (88% forward against 12% back). Nevertheless, the main assumption of this model is the plane-parallel approximation. It greatly simplifies the computations since it allows a 1D treatment. The radiative code requires a density profile $n_H(z)$ for the PDR. For convenience, we used a power-law rise starting at z_0 that is defined as

$$n_H(z) = n_0 \times \left(\frac{z}{z_0}\right)^{\alpha}, \tag{5}$$

where z_0 is the depth at which the density reaches the maximum value n_0 and α is the power-law index. The density remains constant at the maximum value between z_0 and z_1 and then decreases symmetrically. Indeed, models with a rise followed by a constant density do not reproduce the observed decrease of intensity after the peak at longer wavelengths. A lower density is required, and for convenience we adopted a symmetric fall-off. The density profile is shown in Fig. 8.

The four parameters, n_0, α, z_0 and z_1 are free to vary in the fitting, contrary to the radiation field parameters (the radius of the exciting star, its temperature, and its distance from the cloud), which are fixed to give an illumination equal to 2.6×10^4 G_0

in Mathis units, following Marconi et al. (1998). Moreover, because the DustEM code computes the emission per hydrogen atom, it is necessary to make an assumption on the column density to compare our model outputs to the data. It is made through the $l_{\rm PDR}$ parameter, corresponding to the PDR length along the line of sight. It is related to the column density $N_{\rm Htot}(z)$ by $N_{\rm Htot}(z) = n_{\rm H}(z)\ l_{\rm PDR}$, where $n_{\rm H}$ is the density along the line of sight. This is a fifth parameter, which is set to reproduce the emission given a density profile. $l_{\rm PDR}$ has to be compatible with previous measurement of the column density in the Orion Bar. 2×10^{23} cm^{-2} is an order of magnitude given by Johnstone et al. (2003) from SCUBA/JCMT observations at 850 μm.

To take into account the self-absorption by dust, which can be substantial in the NIR, the emerging intensity is reduced by

$$\int_0^{l_{\rm PDR}} \frac{e^{-\tau(\lambda,l)}}{l_{\rm PDR}} {\rm d}l, \tag{6}$$

where l is the distance along the line of sight ($l = 0$ at the PDR edge) and $\tau(\lambda, l)$, the optical depth, computed by assuming no density gradient along the line of sight and using the extinction curve computed by DustEM. This factor is only significant at 3.6 μm since the optical depth is indeed very low at longer wavelengths ($\tau_{\rm max} < 0.4$ at 70 μm). Finally, the model output is convoluted by the appropiate PSF and integrated over each considered filter to be compared to the data.

6.2. Fitting

Several different density profiles have been tested to explore the parameter space and the influence of each parameter on the dust emission profiles. We allowed n_0 to vary between 10^4 and 10^6 cm^{-3} which is the canonical density range for the Orion Bar (Hogerheijde et al. 1995; Tauber et al. 1994). For each n_0 value, several power-law indexes α are considered between 1 (a linear rise of density) and 12 (a very steep profile). z_0 and z_1 are well-constrained by the maximum intensity position in each band and require to be fitted a posteriori given the values of n_0 and α.

The maximum density n_0 affects the overall brightness. The densest is the PDR, the highest is the brightness in *Herschel* bands. For a given n_0 and at a given wavelength, the α power-law index defines where the dust emission peaks. Indeed, the brightness peak position depends on a competition between the incident flux and the density of absorbing particles.There is consequently a degeneracy between n_0 and α and to keep a peak position constant with an increasing density, a higher power-law index is needed. We also notice that the couple (n_0, α) changes the shape of the profiles. On the other hand, the length of the PDR along the line of sight is a multiplicative factor and affects each band in the same way.

Concerning the dust model, we consider the abundances and optical properties of dust in the diffuse ISM. The best adjustment of the data were obtained with the following parameters: $n_0 = 1.5 \times 10^5$ cm^{-3}, $\alpha = 2$, $z_0 = 5.25 \times 10^{-2}$ pc, $z_1 = 6.95 \times 10^{-2}$ pc and $l_{\rm PDR} = 0.45$ pc. Using these parameters we obtain $N_{\rm H} = n_0 \times l_{\rm PDR} = 2 \times 10^{23}$ cm^{-2}, which is of the same order of magnitude as measured by Johnstone et al. (2003). Combining the whole geometry leads to a ridge that is ~0.45 pc long along the line of sight, ~0.05 pc thick (width at half maximum of the density profile) and ~0.42 pc long in the sky plane. Figure 9 compares the observed and modelled brightness profiles. The spatial shift between the maximum intensity positions observed at different wavelengths is satisfactorily reproduced. The absolute brightnesses in the *Herschel* bands are also quite well reproduced by the model, except for the 160 and 250 μm emissions, which are underestimated. The modelled profiles are also narrower than the data and, at shorter wavelengths, the PAH emission is significantly overestimated by the model.

7. Discussion

Using our plane-parallel model of the Orion Bar, assuming dust properties typical for the diffuse atomic ISM and with values of the local and column densities compatible with previous observations, we were able to reproduce the stratification of the dust emission inside the PDR seen in *Herschel* and *Spitzer*/IRAC data very well (Figs. 1 and 6). This indicates that the increase of the distance between the observed Bar and the illuminating star with increasing wavelength is a pure radiative transfer effect. This model is also able to reproduce at first order the general shape of the brightness profiles and the absolute brightness observed with *Herschel*. We conclude that a simple plane-parallel model seems to be a reasonable approximation of the Bar.

The discrepancy between the synthetic and observed brightness profiles in *Herschel* bands can be explained by two assumptions we made. First, the PDR was modelled as a single slab without matter in front and behind, and so the model does not reproduce the observed brightness outside the ridge. Second, the geometry may be not purely edge-on (e.g., Tielens et al. 1993; Wen & O'Dell 1995; Pellegrini et al. 2009). Inclination effects, which are not taken into account in our study, can broaden the brightness profiles and the SEDs. Sub-structures that are ignored in our modelling can also broaden the profiles.

The overestimated PAH emission in the Orion Bar while using diffuse ISM dust abundances is not a surprise and could be caused by several phenomena.

1. Dust grains in the Orion Bar undergo a very hard UV radiation field, which can photo-destroy PAHs at the ionization front (Giard et al. 1994). This could be coupled with PAH sticking on BGs in the molecular cloud (Kim et al. 1994). Reducing the PAH abundance by a factor 7, without changing any other parameter, provides a good match of the 3.6 μm brightness profile (Fig. 10). Less PAHs reduce the UV absorption, and therefore the emission in *Herschel* bands slightly increases (maximum brightness multiplied by factors 1.1−1.2 except at 160 μm where it is unchanged).
2. In a dense medium, where the radiation does not penetrate, dust grains are suspected to be coagulated (Tielens 1989), which increases the overall FIR emissivity $\epsilon_{\rm FIR}$ by factors about 2−3 (e.g., Bernard et al. 1999; Stepnik et al. 2003; Paradis et al. 2009; Köhler et al. 2011). To be in agreement with the observations, a model with an increase of $\epsilon_{\rm FIR}$ must be counterbalanced by a decrease of the column density (through the $l_{\rm PDR}$ parameter) by the same factor. Taking into account this enhancement provides a good match of the brightness profiles, as illustrated in Fig. 11, and a decrease of the length along the line of sight by factor 2−3 is still compatible with observational constraints.
3. The length along the line of sight may be not constant. As mentioned above, in *Herschel* bands we probed the densest part of the Bar, whereas at 3.6 μm we are sensitive to the surface emission, which is very structured (first panel of Fig. 1). What appears as a bar in the sky plane could be a convex surface pointing at the illuminating star, and thus presenting a bigger depth along the line of sight in the densest part than near the ionization front. Photodissociation region models of the gas emission in the Orion Bar focus on the HII region and

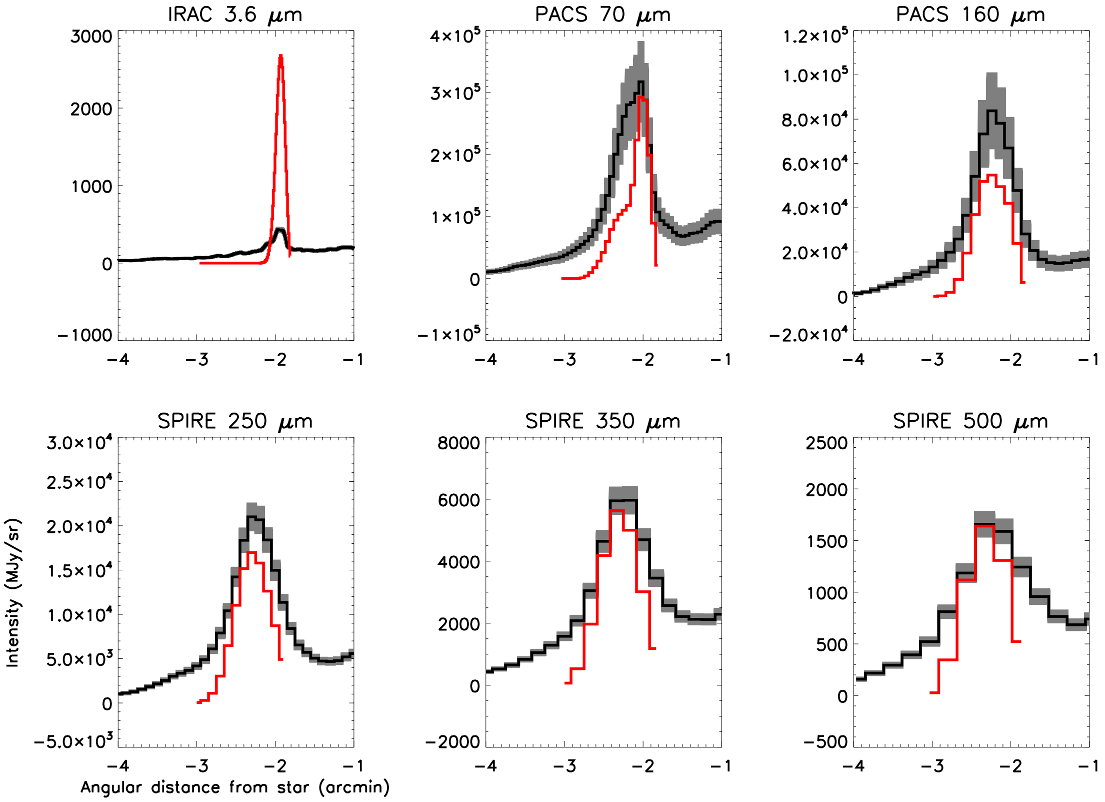

Fig. 9. Brightness profiles from *Spitzer* and *Herschel* observations (black). The photometric uncertainties are 5% for IRAC, 20% for PACS and 7% for SPIRE (grey), respectively. The modelling using diffuse ISM dust properties is shown by the red lines.

Table 2. Properties of the different models.

	$Y_{\rm PAH}$ $(M/M_{\rm H})$	$Y_{\rm SamC}$	$Y_{\rm LamC}$	$Y_{\rm aSil}$	$\epsilon_{\rm FIR}$	$l_{\rm PDR}$(pc)
Diffuse ISM model (Fig. 9)	7.8×10^{-4}	1.65×10^{-4}	1.45×10^{-3}	7.8×10^{-3}	$\epsilon^0_{\rm FIR}(\lambda)^a$	0.45
PAH depleted model (Fig. 10)	1.1×10^{-4}	1.65×10^{-4}	1.45×10^{-3}	7.8×10^{-3}	$\epsilon^0_{\rm FIR}(\lambda)^a$	0.45
PAH depleted model + $\epsilon_{\rm BG}$ enhancement (Fig. 11)	2.36×10^{-4}	1.65×10^{-4}	1.45×10^{-3}	7.8×10^{-3}	$2 \times \epsilon^0_{\rm FIR}(\lambda)^a$	0.25

Notes. [a] $\epsilon^0_{\rm FIR}(\lambda)$ is the FIR emissivity presented in Fig. A.1 from Compiègne et al. (2011).

the zone near the ionization front, and fit the observations considering a length along the line of sight close to 0.15 pc (Pellegrini et al. 2009) while we assumed $l_{\rm PDR}$ = 0.45 pc in our modelling. Therefore, the excess of the 3.6 μm emission in our model could be simply explained by a decrease of the length along the line of sight near the ionization front.

Finally, the observed absolute brightnesses at 160 μm and at 250 μm are underestimated by factors 1.5 and 1.2, respectively. This comes from the dust model itself. With DustEM, optical properties of the BG component, made of silicates and large amorphous carbons, create an emerging spectrum with a value of the spectral emissivity index β close to 1.55. Cooling and radiative transfer cannot change this. As a consequence, we fail to reproduce the SED of BGs, whatever the position on the Bar; grains are systematically cooler and spectra are systematically steeper in the data than in the model, as illustrated at the 70 μm peak position shown in Fig. 12. The SEDs of BGs at different position across the Bar (studied in Sect. 4 and shown in Fig. 5) reveal β values around 1.8 in the Bar. This discrepancy between the model and the data induces the underestimate of β seen in Fig. 12.

8. Conclusion

We have presented the first observations of the Orion Bar photodissociation region using the *Herschel* Space Observatory in five broad bands (70 and 160 μm with PACS, 250, 350 and 500 μm with SPIRE). The wavelength range and the spatial resolution of *Herschel* allow us to map and resolve the emission of the biggest grains that are located in the densest zones of the Orion Bar.

To extract SEDs, we developed an original and efficient method to compute convolution kernels allowing to convert all maps to the same beam. Study of BG SEDs at different positions in the Orion Bar region reveals a cooling of dust (from 70 K to 35 K) and an increase of the spectral emissivity index β (from 1.1 to 2) as we go deep into the PDR. Combining the new *Herschel* observations with ancillary data from *Spitzer*/IRAC gives us the opportunity to probe the morphology of the Orion Bar from 3.6 μm to 500 μm. The overall structure is the same at all wavelengths but we observe an increase in the distance star-Bar with increasing wavelength (shift of ~30″ between the 3.6 μm and the 500 μm profiles), which implies a stratification of dust properties within the Bar. We used a radiative transfer

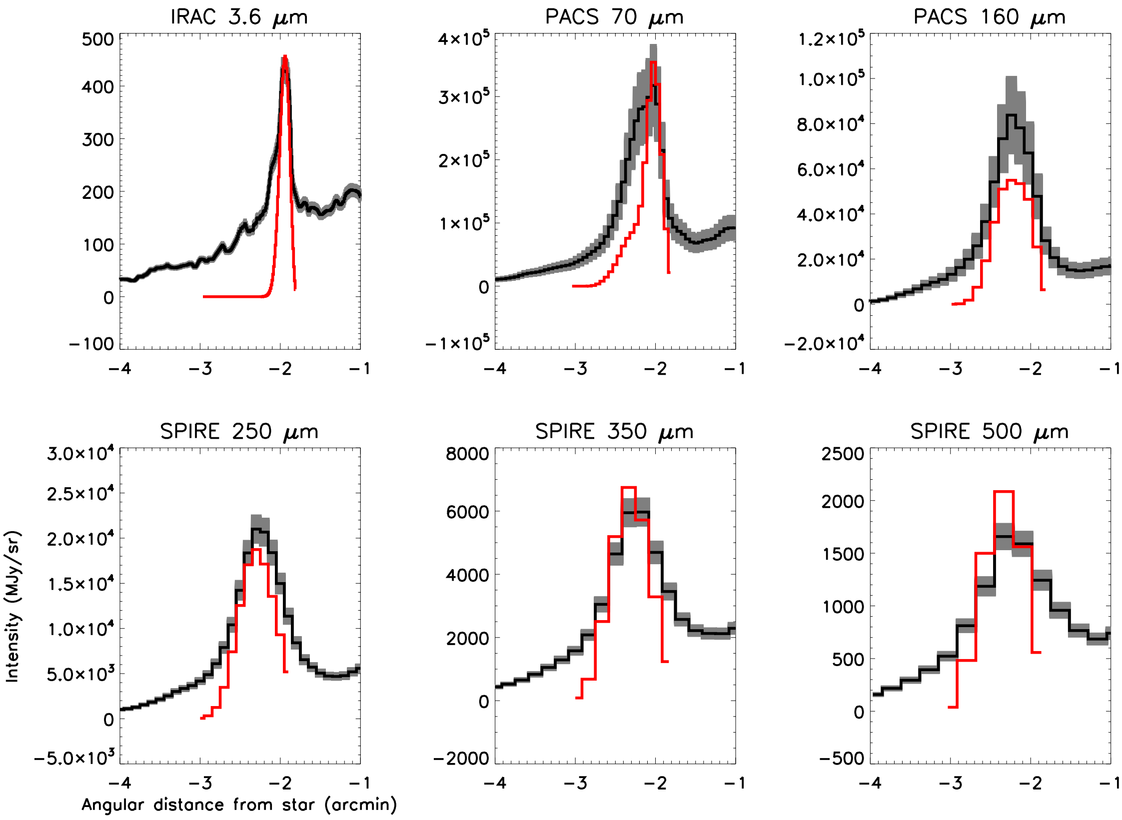

Fig. 10. Same as Fig. 9 with a PAH abundance seven times lower than in the diffuse ISM (Table 2). The increase of brightness in the model at long wavelengths is caused by a weaker absorption in the UV/visible.

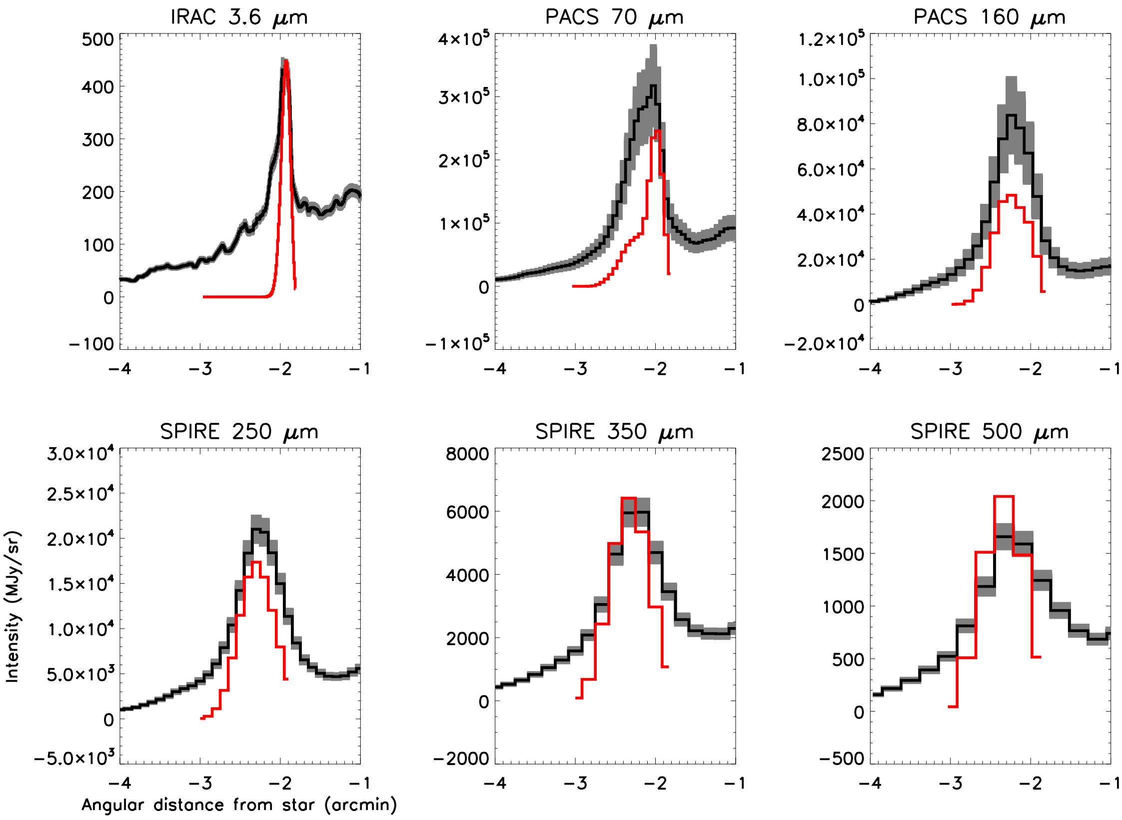

Fig. 11. Same as Fig. 9 with $l_{\rm PDR} = 0.25$ pc. PAH abundance is a factor 3.3 lower than the canonical value in the diffuse ISM. The BG emissivity is enhanced by a factor 2 (Table 2).

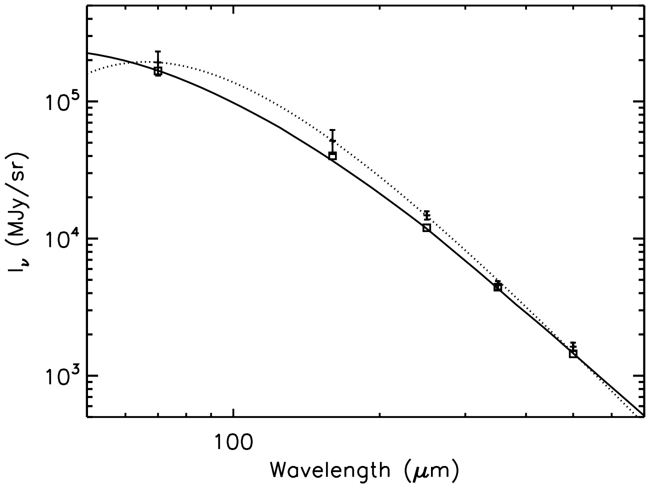

Fig. 12. Solid line: SED extracted from the radiative transfer model using diffuse ISM properties (Table 2) at the 70 μm peak position (Fig. 9). Square: integrated fluxes in *Herschel* bands. Dotted line: modified blackbody fitted to the data.

model using typical diffuse ISM dust properties and abundance to model the brightness profiles observed with *Herschel* and *Spitzer*. This model reproduces the stratification within the Bar using values of the column density and local density parameters that agree with the observational constraints. This shows that this stratification is purely a radiative transfer effect.

However, using diffuse ISM dust properties and abundances in the model leads to several discrepancies in shape and absolute brightness between the modelled brightness profiles and the observations. The assumptions we made about the geometry (considering the PDR as a single slab, adoption of an edge-on geometry, without inclination and sub-structure effects) can explain the differences of width between the synthetic and observed profiles.

The relatively low absolute brightness at 3.6 μm might be explained by PAH photo-destruction by the strong UV radiation, or by sticking of PAHs to the BGs in the pre-existing molecular cloud. A PAH abundance decrease by a factor 7 from the canonical value in the diffuse ISM provides a good fit of the IRAC 3.6 μm emission. A combination of a decreased PAH abundance (by a factor less than 7) with a decreased length along the line of sight is possible as well. If that is the case, an increase of the brightness in *Herschel* bands is needed to fit the data. Coagulation can explain this behaviour since it can enhance the FIR emissivity by factors 2−3. An alternative is that the length along the line of sight is shorter at 3.6 μm since we probed the emission from the surface of dense structures.

Acknowledgements. We thank Laurent Verstraete and Mathieu Compiègne for useful discussions about the DustEM model. HIPE is a joint development by the *Herschel* Science Ground Segment Consortium, consisting of ESA, the NASA *Herschel* Science Center, and the HIFI, PACS and SPIRE consortia. PACS has been developed by a consortium of institutes led by MPE (Germany) and including UVIE (Austria); KU Leuven, CSL, IMEC (Belgium); CEA, LAM (France); MPIA (Germany); INAF-IFSI/OAA/OAP/OAT, LENS, SISSA (Italy); IAC (Spain). This development has been supported by the funding agencies BMVIT (Austria), ESA-PRODEX (Belgium), CEA/CNES (France), DLR (Germany), ASI/INAF (Italy), and CICYT/MCYT (Spain). SPIRE has been developed by a consortium of institutes led by Cardiff University (UK) and including Univ. Lethbridge (Canada); NAOC (China); CEA, LAM (France); IFSI, Univ. Padua (Italy); IAC (Spain); Stockholm Observatory (Sweden); Imperial College London, RAL, UCL-MSSL, UKATC, Univ. Sussex, STFC, UKSA (UK); and Caltech, JPL, NHSC, Univ. Colorado (USA). This development has been supported by national funding agencies: CSA (Canada); NAOC (China); CEA, CNES, CNRS (France); ASI (Italy); MCINN (Spain); SNSB (Sweden); STFC (UK); and NASA (USA).

References

Abergel, A., Arab, H., Compiègne, M., et al. 2010, A&A, 518, L96
Ali, B. 2011, PACS technical note, https://nhscdmz2.ipac.caltech.edu/pacs/docs/Photometer/
Aniano, G., Draine, B. T., Gordon, K. D., & Sandstrom, K. 2011, PASP, 123, 1218
Bernard, J. P., Abergel, A., Ristorcelli, I., et al. 1999, A&A, 347, 640
Bernard-Salas, J., Habart, E., Arab, H., et al. 2012, A&A, 538, A37
Buckle, J. V., Davis, C. J., Di Francesco, J., et al. 2012, MNRAS, in press [arXiv:1201.5483]
Compiègne, M., Abergel, A., Verstraete, L., & Habart, E. 2008, A&A, 491, 797
Compiègne, M., Verstraete, L., Jones, A., et al. 2011, A&A, 525, A103
Desert, F., Boulanger, F., & Puget, J. L. 1990, A&A, 237, 215
Dicker, S. R., Mason, B. S., Korngut, P. M., et al. 2009, ApJ, 705, 226
Draine, B. T., & Li, A. 2007, ApJ, 657, 810
Giard, M., Bernard, J. P., Lacombe, F., Normand, P., & Rouan, D. 1994, A&A, 291, 239
Goicoechea, J. R., Joblin, C., Contursi, A., et al. 2011, A&A, 530, L16
Gonzalez, R. C., & Woods, R. E. 1992, Digital Image Processing, 3rd edn. (Addison-Wesley Pub (Sd))
Griffin, M. J., Abergel, A., Abreu, A., et al. 2010, A&A, 518, L3
Habing, H. J. 1968, Bull. Astron. Inst. Netherlands, 19, 421
Hogerheijde, M. R., Jansen, D. J., & van Dishoeck, E. F. 1995, A&A, 294, 792
Johnstone, D., Boonman, A. M. S., & van Dishoeck, E. F. 2003, A&A, 412, 157
Kim, S.-H., Martin, P. G., & Hendry, P. D. 1994, ApJ, 422, 164
Köhler, M., Guillet, V., & Jones, A. 2011, A&A, 528, A96
Lis, D. C., & Schilke, P. 2003, ApJ, 597, L145
Marconi, A., Testi, L., Natta, A., & Walmsley, C. M. 1998, A&A, 330, 696
Markwardt, C. B. 2009, in Astronomical Data Analysis Software and Systems XVIII, ed. D. A. Bohlender, D. Durand, & P. Dowler, ASP Conf. Ser., 411, 251
Mathis, J. S., Mezger, P. G., & Panagia, N. 1983, A&A, 128, 212
Menten, K. M., Reid, M. J., Forbrich, J., & Brunthaler, A. 2007, A&A, 474, 515
Paradis, D., Bernard, J.-P., & Mény, C. 2009, A&A, 506, 745
Pellegrini, E. W., Baldwin, J. A., Ferland, G. J., Shaw, G., & Heathcote, S. 2009, ApJ, 693, 285
Pilbratt, G. L., Riedinger, J. R., Passvogel, T., et al. 2010, A&A, 518, L1
Poglitsch, A., Waelkens, C., Geis, N., et al. 2010, A&A, 518, L2
Sibthorpe, B., Ferlet, M., Bendo, G., & Papageorgiou, A. 2011, SPIRE release note, ftp://ftp.sciops.esa.int/pub/hsc-calibration/SPIRE/PHOT/Beams/
Stepnik, B., Abergel, A., Bernard, J., et al. 2003, A&A, 398, 551
Tauber, J. A., Tielens, A. G. G. M., Meixner, M., & Foldsmith, P. F. 1994, ApJ, 422, 136
Tielens, A. 1989, in Interstellar Dust, ed. L. J. Allamandola, & A. G. G. M. Tielens, IAU Symp., 135, 239
Tielens, A. G. G. M., & Hollenbach, D. 1985, ApJ, 291, 722
Tielens, A. G. G. M., Meixner, M. M., van der Werf, P. P., et al. 1993, Science, 262, 86
Tikhonov, A. 1963, in Soviet Math. Doklady, 4, 1035
van der Werf, P. P., Stutzki, J., Sternberg, A., & Krabbe, A. 1996, A&A, 313, 633
Walmsley, C. M., Natta, A., Oliva, E., & Testi, L. 2000, A&A, 364, 301
Wen, Z., & O'Dell, C. R. 1995, ApJ, 438, 784
White, G. J., & Sandell, G. 1995, A&A, 299, 179
Witt, A. N., Friedmann, B. C., & Sasseen, T. P. 1997, ApJ, 481, 809
Young Owl, R. C., Meixner, M. M., Wolfire, M., Tielens, A. G. G. M., & Tauber, J. 2000, ApJ, 540, 886
Zubko, V., Dwek, E., & Arendt, R. G. 2004, ApJS, 152, 211